remote sensing

MDPI

Article

Accelerating Deep Learning in Radar Systems: A Simulation Framework for 60 GHz Indoor Radar

Philipp Reitz *, Timo Maiwald, Jonas Bönsch, Norman Franchi and Maximilian Lübke

Institute for Smart Electronics and Systems, Friedrich-Alexander-Universität Erlangen-Nürnberg, 91058 Erlangen, Germany; timo.maiwald@fau.de (T.M.); jonas.boensch@fau.de (J.B.); norman.franchi@fau.de (N.F.); maximilian.luebke@fau.de (M.L.)

* Correspondence: phil.reitz@fau.de

Abstract: FMCW radar systems are increasingly used in diverse applications, and emerging technologies like JCAS offer new opportunities. However, machine learning for radar faces challenges due to limited application-specific datasets, often requiring advanced simulations to supplement real-world data. This paper presents a setup for generating synthetic radar data for indoor environments, evaluated using CNNs. The setup involves comprehensive modeling, including far-field antenna simulations, variations in human radar cross-section, and detailed representations of indoor environments with their corresponding propagation channel properties. These synthetic data are used to train CNNs, and their performance is assessed on real measurement data. The results demonstrate that CNNs trained on synthetic data can perform well when tested on real measurement data. Specifically, the models trained with synthetic data showed performance comparable to models trained with real measurement data, which required a minimum of 300 samples to reach similar levels of accuracy. This result demonstrates that synthetic data can effectively train neural networks, providing an alternative to real measurement data, particularly when collecting sufficient real-world samples is difficult or costly. This approach significantly reduces the time required for generating datasets, and the ability to quickly label data in simulations simplifies and accelerates post-processing. Additionally, the generated datasets can be made more heterogeneous by introducing varying signal conditions, enhancing the diversity and robustness of the training data.

Keywords: convolutional neural network; FMCW radar; mm-wave; radar cross section; simulation and measurement

check for updates

Citation: Reitz, P.; Maiwald, T.; Bönsch, J.; Franchi, N.; Lübke, M. Accelerating Deep Learning in Radar Systems: A Simulation Framework for 60 GHz Indoor Radar. *Remote Sens.* **2024**, *16*, 4028. https://doi.org/10.3390/rs16214028

Academic Editor: Konrad Jędrzejewski

Received: 4 October 2024
Revised: 23 October 2024
Accepted: 28 October 2024
Published: 30 October 2024

Copyright: © 2024 by the authors. Licensee MDPI, Basel, Switzerland. This article is an open access article distributed under the terms and conditions of the Creative Commons Attribution (CC BY) license (https://creativecommons.org/licenses/by/4.0/).

1. Introduction

Radar sensors have experienced increasing interest in recent years due to their variety of applications and robustness compared to other sensor types [1–3]. Frequency Modulated Continuous Wave (FMCW) radar systems, in particular, have gained prominence for their capability to measure distances, relative velocities, and angles of arrival. These systems are available as single-chip solutions, offering significant integration advantages and facilitating their use in automotive, industrial, healthcare, and smart home environments. Joint Communication and Sensing (JCAS) and Integrated Communication and Sensing (ICAS) are potential new technologies for future mobile communication generations, offering new application areas by integrating radar into mobile networks [4–6]. Alongside the rapid development of radar systems, machine learning has been used to enhance radar applications. Compared to image classification, which benefits from extensive public datasets, developing reliable machine learning algorithms for radars requires customized datasets, which are commonly unavailable or unsuitable for the respective application [7,8]. Existing datasets are primarily derived from the automotive sector. A significant reason is likely the great variety of radar sensors with different operation frequencies, antenna patterns, etc. High-quality data, a good representation of application scenarios, and a sufficient data set size characterize an adequate machine learning (ML) dataset. Creating these datasets for

real-world applications is extremely challenging, time-consuming, and costly [8]. However, ML algorithms can be trained and developed using synthetic data to augment real-world datasets or supplement measurements. Advanced simulation tools like CST, Feko, Python, or Matlab enable realistic simulations of millimeter wave characteristics at different stages of development. With software tools becoming increasingly powerful, simulations of complex application scenarios, including human movements in realistic environments, are made possible [9–11].

In this paper, we introduce a workflow for generating synthetic datasets designed for indoor radar sensing at 60 GHz, as illustrated in Figure 1. The data pipeline is based on Blender, CST, Feko, WinProp, and Python simulation tools. Blender is used for mesh modeling, while electromagnetic field simulations use the field solvers CST and Feko. CST Studio Suite specializes in full-wave 3D simulations for high-frequency applications like antenna design, using finite element method solvers. Feko, on the other hand, focuses on antenna performance, Radar Cross Section (RCS) analysis, and electromagnetic compatibility, utilizing the method of moments and hybrid solvers for large-scale and complex scenarios. Building on their results, the electromagnetic field simulation of millimeter waves is conducted in WinProp. Signal processing and the simulation of electrical components can be carried out in Python. The foundation of the data generation process is radar target modeling. Two approaches are investigated: the first involves monostatic RCS simulation, while the second focuses on generating a high-resolution mesh integrated into the ray tracing process. Precise target modeling using monostatic RCS information is achieved through Feko. This information is imported into WinProp, where channel modeling is performed. The second approach involves modeling targets as meshes in Blender, which are subsequently imported into WinProp. After object modeling, channel modeling is conducted in WinProp, simulating the physical propagation characteristics of millimeter waves. The simulation of the antenna patterns is carried out in CST Studio, and these patterns are considered for ray tracing of millimeter waves at both the transmitting and receiving antennas. The subsequent radar signal processing for the linear sawtooth chirp is implemented following the state-of-the-art method in Python. The entire development chain can be simulated, from antenna design to final deployment, allowing data collection without real hardware.

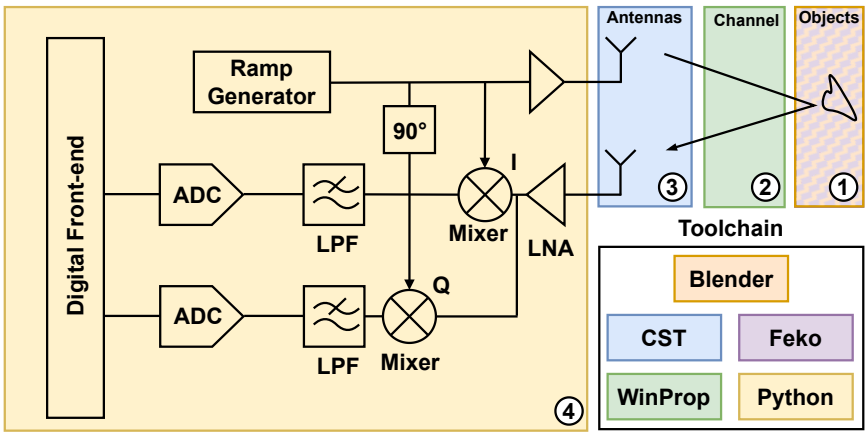


Figure 1. Simulation toolchain for generating synthetic radar data using Blender, Feko, CST, WinProp, and Python, covering: 1. object and backscattering modeling, 2. channel propagation modeling, 3. Antenna design, and 4. analog and digital signal processing.

In this paper, we evaluate the effectiveness of our toolchain for generating synthetic datasets to train convolutional neural networks (CNNs). Nonlinearities in system components, noise, interference behavior variations, and complex reflection scenarios represent discrepancies that simulations may not fully capture. The focus of this study is to assess the impact of these deviations on the design and performance of CNNs, determining their

significance in ensuring accurate and robust model training. The main contributions of this paper are summarized as follows:

- This paper presents a simulation chain for generating synthetic monostatic 60 GHz FMCW radar datasets in indoor environments, starting with antenna design and extending to environment simulation using WinProp for a full physical propagation simulation. This approach considers millimeter wave propagation characteristics, enabling the creation of realistic datasets for developing and testing radar systems and ML algorithms for object detection in indoor environments.
- The simulation results of the range-power profile, obtained from both ray tracing and monostatic RCS simulations, are compared with actual measurements. This comparison aims to evaluate the accuracy of the simulated profiles against real-world data.
- The impact of data quantity on the performance of a CNN model for range detection using range-Doppler analysis in a specific indoor environment is explored. The discussion highlights the potential benefits of synthetic datasets in enhancing ML performance for the selected setup. The study addresses the trade-offs between dataset size and model accuracy, emphasizing how synthetic data can supplement limited real-world measurements.

This article is an expanded version of a paper entitled "Evaluating Synthetic Data Potential for 60 GHz FMCW Radar Simulations with Real Measurements", which was presented at the International Radar Symposium, Poland (July 2024) [12]. The expanded article provides a more in-depth analysis of the datasets and demonstrates the successful ML transfer from synthetic data to real-world data. It further explores dynamic simulations for target detection using CNNs, investigating the effects of different dataset sizes and conditions on detection performance. Additionally, we discuss the practical implications of transferring models trained on synthetic data to real-world scenarios, offering insights into both the benefits and limitations of this approach.

2. Related Work

The increasing use of radars for different kinds of applications raises the demand for complex simulations as applications become more diverse and challenging. Some powerful frameworks have been proposed, including real-time raw data, antenna patterns, and various sensor configurations [13–15]. Since several aspects come into play, published works either focus on specific elements of radar simulations in greater detail, such as RCS simulations [16–19], environment simulations [14,20], or direction of arrival simulations [21,22], or cover studies with multiple aspects [23,24]. This work focuses on generating large synthetic datasets that resemble the structure of actual measurement data. Various simulation concepts are proposed in the literature for generating datasets. Ray tracing, artificial target lists, path delay, and skeletal tracking are the most commonly used concepts. Transferring the trained model to unseen measurement data is essential to assess its performance. Datasets can be categorized into fully synthetic datasets, hybrid models, or measurements only. Fully synthetic datasets are generated without measurements, making them easy to label and scale. Measurements are involved in some form in hybrid datasets, making them closer to real-world data but more complex to scale in quantity. Additionally, we classify the literature based on the radar data used: range-Doppler maps (RDM), range-angular maps (RAM), micro-Doppler (μD), and radar waveforms (WF). Table 1 summarizes the proposed concepts in the literature.

Table 1. Overview of research approaches for generating and validating synthetic datasets.

Reference	Application	Simulation Approach	Transfer	ML Data Set	Type of ML	Data Format	Year
[25]	Gesture recognition	Artificial target list	Yes	Hybrid	CNN	µD	2024
[26]	Object detection	Ray tracing	Yes	Hybrid	AE	RAM	2023
[27]	Gesture recognition	Ray tracing	Yes	Fully syn.	ResNet	RAM	2024
[28]	Posture estimation	Skeletal tracking	No	Hybrid	CNN	RAM	2020
[29]	RCS classification	Physical optics method	Yes	Fully syn.	ANN, CNN	RAM	2021
[30]	Waveform classification	Waveform-based	No	Fully syn.	CNN	WF	2021
[31]	Object Detection and Classification	Ray tracing	No	Fully syn.	CNN	RDM	2021
[32]	Human activity recognition	Path delay	No	Fully syn.	DCNN	µD	2024
[33]	Personnel security screening	Physical Model	No	Hybrid	DCNN	RAM	2023
[34]	Posture tracing	EM simulations	Yes	Fully syn.	GAN	RAM	2023
[35]	Automotive radar	bidirectional ray tracing	No	Fully syn.	CNN	RDM	2023
This work	Indoor Object detection	Full Physical Simulation	Yes	Fully syn.	CNN	RDM	2024

Zhou et al. summarize and compare published datasets in [36] and manage an overview of the GitHub repository in [37]. They differentiate between conventional radar datasets for autonomous driving (8 instances), pre-CFAR datasets for detection (6 instances), 4D radar datasets (8 instances), specific tasks (17 instances), odometry and localization (10 instances), gestures (5 instances), human activity and reconstruction (6 instances), and vital sign datasets (3 instances). Used operating frequencies vary between 5.8 GHz and 77 GHz. Data types such as IQ or ADC data, point clouds, range-Doppler, or range-angle maps often make it challenging to use them for customized applications. For this reason, creating new datasets tailored to specific requirements is usually necessary.

Our work presents a workflow for generating fully synthetic datasets for indoor localization, considering the propagation and attenuation properties of millimeter waves through ray tracing. The performance of the trained ML model is then evaluated on an unseen test dataset determined through measurements.

3. Methods

This section describes the simulation environment, radar hardware for simulation and measurements, and solver settings. The structure of the following section sticks to the numbering of the simulation blocks presented in Figure 1 in the subsequent subsections: (1) objects, (2) channel, (3) antennas, (4) radar hardware and signal processing. The performance of CNNs in range detection of moving targets based on range-Doppler maps with increased multipath propagation is evaluated. The primary objective is to assess how different datasets impact the effectiveness of CNNs for this specific task. The simulation framework starts with an antenna simulation of the patch array based on a Texas Instruments AWR6843ISK radar (Texas Instruments, Dallas, TX, USA) evaluation board

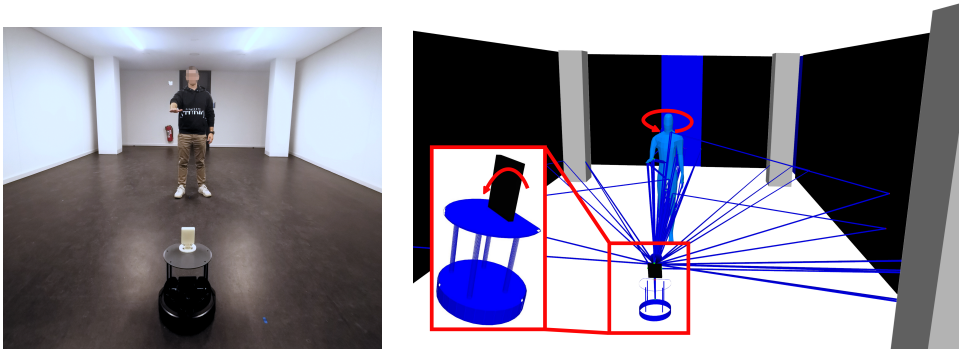
conducted in CST. Subsequently, a radar cross-section simulation is performed in Feko, Altair, followed by an environment simulation in WinProp, Altair. Radar signal processing is performed in a separate simulation framework using Python (Version 3.11.5). This holistic simulation approach enhances the quality of the simulation and provides a deeper understanding of propagation effects.

3.1. Environment and Target Modeling

Radar reflection paths can be simulated using various methods, including artificial target lists, ray tracing, multi-body simulations, and scattering simulations. This paper employs mesh modeling for the environment in Section 3.1.1 and detailed RCS modeling and mesh modeling for the target in Section 3.1.2. Additionally, Section 3.1.2 discusses how the obtained dynamic reflection paths can be scaled up for the generation of large datasets.

3.1.1. Environment

To simulate the complexities of real-world object detection, the clutter level caused by the multipath of the environment must be reproduced in detail. Therefore, different synthetic radar echoes must be generated simultaneously to model complex scenarios [24]. A detailed CAD model of the indoor environment (Figure 2) was used for this purpose. In the measurement, a radar testing environment with 5.50 m $\times$ 9.50 m was selected. Figure 2a presents the radar testing room, while Figure 2b shows the simulation setup and the scenario replication in the ray tracing program WinProp. Reflections are shown in blue for visualization purposes. This visualization demonstrates the interactions between transmitted radar signals, the human target, and its surrounding environment. Furthermore, Figure 2b illustrates the variation in the tilt angle of the radar board as well as the pedestrian's direction of rotation. Minimal changes in the radar board's rotational angle or the pedestrian's tilt angle result in altered reflection properties. The following chapter will discuss a detailed model of the human as a radar target. The room's corners are characterized by a supporting pillar structure that causes additional multipath reflections in measurements and simulations. The geometric dimensions of the room are modeled with high accuracy in a CAD model, taking into account both the floor and the ceiling. The room has only the wall, the pillar structure, the floor, and the ceiling as scattering objects. These structures reduce the complexity of multipath reflections and enable simplified reproduction in simulation models. Mounted on a robot at a height of 0.50 m, the radar was oriented directly toward a pedestrian. The radar was tilted upwards by 20° to optimize target detection. This tilt was adjusted to maximize the probability of detection by aligning the sensor with the typical height and position of a human target.



(**a**) Real environment (**b**) Simulation environment (WinProp)

Figure 2. Comparison of (**a**) real environment and (**b**) simulated radar environment in WinProp (Reprinted with permission from [12] 'IEEE 2024').

3.1.2. Target

This chapter examines two approaches for target modeling: Mesh and RCS modeling. Modeling the target using a geometric mesh allows fast computation but neglects volatile

behavior due to interference effects. On the other hand, modeling the radar target using monostatic RCS information offers more detail, as the mesh is refined explicitly to the wavelength to account for interference effects.

Geometric Mesh Modeling for Human Targets

Table 2 presents the fundamental parameters of the mesh geometry for a human target used in radar simulations. The number of vertices, edges, and faces defines the mesh structure, with 3300 triangles representing the discretized surface of the model. The human target model, with dimensions of 0.497 m (X), 0.705 m (Y), and 1.92 m (Z), reflects human proportions. Combined with the detailed mesh structure, these dimensions provide a basis for simulating radar scattering effects while maintaining a balance between accuracy and computational demands.

Table 2. Mesh configuration for human targets in standing and walking positions.

Parameter	Human Walking Pose	Human Standing Pose
Vertices	1652	1652
Edges	3310	4950
Faces	1660	3300
Triangles	3300	3300

Radar Cross Section Modeling for Human Targets

Calculating the RCS can increase the accuracy of ray tracing results. Mono- and bistatic RCS simulations using Feko have been validated in [38–42]. The end-to-end performance has been validated in [43]. On the other hand, simulation tools like Feko can accelerate simulations of complex geometries. The human model is additionally remeshed in Feko to calculate the RCS. The number of triangles, the average edge length, the standard deviation of the edge length, and the minimum and maximum of the edge length are summarized in Table 3. This paper uses the ray launching geometrical optics (RL-GO) solver to calculate the RCS, which is an asymptotic high-frequency computational solver optimized for analyzing electrically large dielectric structures $> 20\lambda$ in scale [44].

Table 3. Mesh metrics for model and simulation evaluation.

Mesh Metrics	Unit	Model Mesh	Simulation Mesh
Triangles	-	3300	3748
Average edge length	mm	33.39	31.88
Standard deviation	mm	26.69	17.23
Minimum edge length	mm	2.698	3.676
Maximum edge length	mm	137.4	133.3

Calculating the entire hemisphere around the human model is not of interest to the specific detection requirements since only one specific observation angle is considered. Therefore, only a part of the hemisphere of the RCS is calculated. This allows to conduct a more efficient simulation by focusing on the most relevant angles for human detection. Material parameters for skin, particularly electrical conductivity and relative permittivity, are chosen for a frequency of 60 GHz. According to Chen et al., in [45], the errors due to clothing are minor, as dry clothing only slightly dampens millimeter waves. Investigations in [46,47] have also shown a low influence of regular clothing, such as sweaters. The parameters for the RCS calculation are presented in Table 4.

Table 4. Configuration parameters for radar cross section solver.

Parameter	Unit	Value
Theta (θ)	deg	90 to 140
Phi (ϕ)	deg	−55 to 55
Increment Theta ($\Delta\theta$)	deg	0.5
Increment Phi ($\Delta\phi$)	deg	0.5
Polarisation	-	Linear
Skin-Relative Permittivity (ϵ_r)	$\frac{\mathrm{As}}{\mathrm{Vm}}$	10.26
Skin-Conductivity (σ)	$\frac{\mathrm{S}}{\mathrm{m}}$	39.519

Scalable Processing of Dynamic Radar Data

A dynamic simulation of the human target with a specific velocity was set up in WinProp. For each time step, reflections with Doppler shift are calculated, resulting in dynamic outcomes for a trajectory. Each ray in ray tracing possesses a unique angle of arrival, which leads to a Doppler shift that varies according to this angle. The Doppler shift for each ray can be determined based on the absolute speed of the target ($\mathbf{v_0} = 1\,\mathrm{m/s}$), the angle of arrival (θ) and the wavelength (λ) with

$$\mathbf{f_d} = \frac{2\mathbf{v_0}}{\lambda}\cos(\theta). \tag{1}$$

Ten velocity profiles are generated to generate a sufficient number of velocity variations. Since the noise and the noise distribution vary significantly between the frames, the normalized power profile also varies, which prevents only the reflection paths from being shifted on the velocity axis. The Doppler shift $\mathbf{f_{d,1}}$ calculated for the initial speed $\mathbf{v_1}$ can be scaled to obtain a new Doppler shift $\mathbf{f_{d,L}}$ for the adjusted speed $\mathbf{v_L}$. Thus, the Doppler shift for different velocity profiles $\mathbf{f_{d,L}}$ can be adjusted out of the initial Doppler shift $\mathbf{f_{d,0}}$ arbitrarily without starting a new ray tracing process, as described by the following equation:

$$\mathbf{f_{d,L}} = \mathbf{f_{d,0}} \cdot \mathbf{L}. \tag{2}$$

Since the trajectory can be traversed at different speeds, the Doppler shift is scaled using a scaling vector $\mathbf{L}$ to synthesize various speeds. As a result, different speed profiles are available. This approach does not require individual ray tracing for different Doppler shifts, which is time-consuming. Instead, the results of the ray tracing, which contain the geometric propagation properties of the individual rays, are loaded, and the Doppler shift is upscaled during post-processing. Consequently, the vector $\mathbf{L}$ is obtained to scale the individual results up and down. k represents the discretization stages of the absolute velocity profile so that the vector $\mathbf{L}$ can be expressed as

$$\mathbf{L} = \{-1 + 0.2k \mid k \in \{0, 1, 2, \ldots, 10\}\}. \tag{3}$$

The scaling factor $\mathbf{L}$ allows for efficient adjustment of the Doppler shift across different velocities without recalculating ray tracing. This method applies the linear relationship between velocity and Doppler shift, ensuring computational efficiency. At the same time, noise is added separately, ensuring realistic simulation across varying velocity and noise conditions.

3.2. Channel Modeling

3.2.1. Material Parameters

The simulation environment considers the electromagnetic material properties to model the interaction of millimeter waves with different surfaces and structures, as detailed in references [48,49]. The radar's Printed Circuit Board (PCB) was assumed to be metallic, human skin was represented by dry skin, and the walls were modeled using concrete. Glass and wooden doors were simulated with their respective materials. The assigned material

properties, including dielectric permittivity, magnetic permeability, electrical conductivity, surface roughness, and thickness, are summarized in Table 5.

Table 5. Electromagnetic material properties for 60 GHz millimeter wave propagation based on [48,49].

	Unit	Metal	Skin	Concrete	Glass	Wood
Permittivity	$\frac{As}{Vm}$	1	10.26	5.25	6.32	1.99
Permeability	$\frac{Vs}{Am}$	20	1	1	1	1
Conductivity	$\frac{S}{m}$	$10 \cdot 10^6$	39.519	1.136	0.876	0.378
Roughness	mm	0	0	1	0	0.3
Thickness	cm	1	0.1	10	1	1

Ideal smoothness was assumed for metal, human skin, and glass materials. This is based on the premise that the surface roughness of these materials is either negligible or has no practical relevance in this context. Given a low penetration depth of 60 GHz millimeter waves presented in [50], the thickness of human skin is set to 0.1 cm. These assumptions allow for more precise modeling of the interactions between millimeter waves and the different materials under given circumstances.

3.2.2. Ray Tracing Methodology and Simulation Parameters

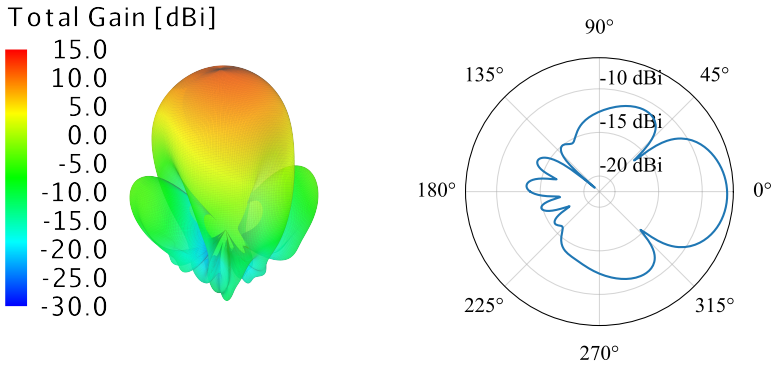
To ensure accurate simulation results, the number of simulated rays should be maximized within computational constraints, as the divergence of rays with increasing distance necessitates a sufficient number of rays for adequate representation. WinProp offers three distinct ray tracing methodologies: intelligent ray tracing, standard ray tracing, and the shooting and bouncing rays technique. Standard ray tracing settings from WinProp are applied for this simulation, simulating the strongest 500 rays. Respective rays are calculated up to a maximum attenuation of 200 dB with a dynamic range of 100 dB per pixel. The number of transmissions, reflections, and diffractions are chosen to run simulations with reasonable computational effort. Parameters used for ray tracing are summarized in Table 6.

Table 6. Parameters for millimeter wave ray tracing using WinProp.

Parameter	Unit	Amount
Number of Rays	-	500
Max. Reflections and Diffractions	-	3
Max. Transmissions	-	3
Max. Reflections	-	2
Max. Diffractions	-	2
Max. Path Loss of Rays	dB	200
Max. Dynamic Range per Pixel	dB	100

3.3. Antenna Parameters

The radar antenna pattern was simulated with CST Studio Suite (Version: 2023) using the frequency domain solver on Rogers RO4835 material (Rogers Corporation, Chandler, AZ, USA). According to the reference design provided by Texas Instruments, a single series fed microstrip patch antenna array is used since conducted measurements use time division multiplexing (TDM) with three transmit and four receive antennas, creating a multiple-input multiple-output (MIMO) system. Results of the far-field simulations are presented in Figure 3. Important parameters are summarized in Table 7.



(**a**) Radiation Pattern (**b**) Elevation Gain

Figure 3. (**a**) Far−field simulation results at 60 GHz from a single series-fed microstrip patch antenna array, modeled in CST, and (**b**) polar representation of the elevation direction featuring a theta cut at $\theta = 0^\circ$ (reprinted with permission from [12] 'IEEE 2024').

Table 7. Parameters for the simulated patch antenna array.

Parameter	Unit	Value
Operating Frequency	GHz	60–64
RX Antennas	-	4
TX Antennas	-	3
Azimuth Angular Resolution	°	15
Elevation Angular Resolution	°	58
Azimuth 3 dB Angular Width	°	75
Elevation 3 dB Angular Width	°	35
Main Lobe Magnitude	dBi	9
Azimuth Side Lobe Level	dB	−26.1
Elevation Side Lobe Level	dB	−15.5

3.4. Radar System Setup and Configuration

Two different configurations were examined to address both static and dynamic target situations. The static examination refers to the position of the robot. In contrast, the dynamic target measurement is conducted at a height of 1.5 m, with a radar configuration adapted to the dynamic situation. The radar's height was adjusted because the ground truth data were manually labeled. In the simulation, the ground truth corresponds to the exact center of the body. A different angle would result in an oblique view of the person, complicating detection and making it difficult to compare with the simulation results. Therefore, maintaining a height of 1.5 m ensures that the radar data aligns with the simulation, where the target's center is consistently captured.

3.4.1. Radar System Design

Radar signal processing follows the state-of-the-art signal processing chain of a linearly modulated fast chirp sequence radar. All chirps are parameterized in the same way. Processing steps and a description of all parameters relevant to the signal processing can be found in [51]. Once data from the whole frame is received, a radar data cube is arranged to perform signal processing steps such as mean filtering, windowing, and applying FFTs to obtain range profiles and range-Doppler plots. In dynamic simulations, static clutter removal is applied to dynamic target measurements to improve detection accuracy by eliminating background clutter.

3.4.2. Radar Configuration

The echo signal received from a target usually has two types of noise: noise received through the antenna from external sources and that generated in the radar receiver itself.

Internal noise sources include *thermal noise*, *shot noise*, *partition noise*, and *flicker noise*. Thermal noise usually is dominant [52]. Since most radars can be assumed to operate at a standard temperature, the thermal noise can be minimized by the white power spectrum. The I and Q noise channels are both zero-mean Gaussian random processes with equal power [53]. A Gaussian-distributed noise floor with a defined standard deviation σ_{noise} and mean value μ_{noise} was implemented in the simulation framework to represent the hardware-generated noise. These values are expressed as percentages of the maximum signal strength, with the mean values representing cross-talk components that occur in real measurements due to interference between the transmitting and receiving antennas. We can replicate the measurement conditions more accurately by including these phenomena in the simulation. The noise distribution properties were selected based on Table 8, as they closely align with the average measurement results.

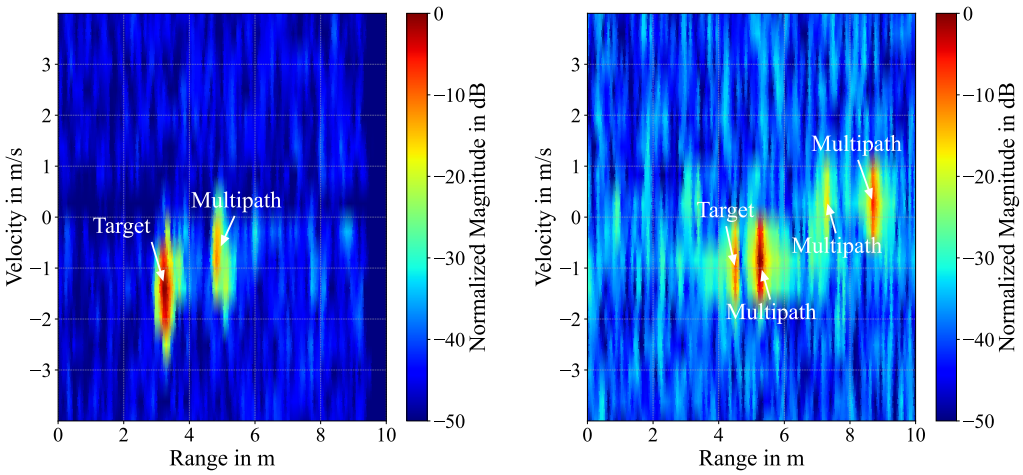
Table 8. Radar system configuration and noise characteristics.

Parameter	Unit	Value
Carrier Frequency	GHz	60
Bandwidth	GHz	3.990
Number of Chirps	-	16
Frame Periodicity	ms	200
Idle Time	µs	50
Chirp Time	µs	50
Slope	GHz/ms	79.8
FFT Size Range	-	128
FFT Size Doppler	-	16
Random Variable (U)	-	$\sim$ Uniform$(0, 2)$
Mean Noise (μ_{noise})	-	$0.01 \cdot U$
Standard Deviation Noise (σ_{noise})	-	$0.0075 \cdot U$
Sampling Frequency (static)	MHz	3.640
Sampling Frequency (dynamic)	MHz	5.460

3.5. CNN for Single-Object Detection in Cluttered Range-Doppler Environments

3.5.1. CNN-Based Target Detection in Multipath Cluttered Range-Doppler Maps

Due to the low attenuation properties of millimeter waves at 60 GHz, multipath propagation frequently occurs, posing a challenge for precise radar detection. Multipath reflections can reduce the radar system's sensitivity and trigger false alarms. In traditional radar signal processing, individual targets are first detected using a CFAR algorithm, followed by a clustering step. The developed ML model aims to replace both steps with a single CNN model that directly predicts the ground truth of the object. To evaluate the performance of the proposed CNN model and synthetic dataset for target detection and range extraction, we select the task of identifying the human target's distance from processed range-Doppler plots while mitigating multipath effects. Figure 4 shows the range-Doppler map of the measurement and the synthetically generated range-Doppler map. Since the noise floor, micro-Doppler and multipath conditions can vary significantly between two measurement frames, comparing the measurement and simulation data is shown for two different time steps but with approximately the same noise level.



(**a**) Real environment (**b**) Simulation in WinProp

Figure 4. Range-Doppler maps showing a moving human with multipath clutter at different time steps: (**a**) measured data and (**b**) WinProp simulations. The comparison focuses on the overall data quality rather than a direct comparison of a specific individual time step, highlighting the alignment between the simulated and measured data in capturing critical characteristics of the scene.

3.5.2. CNN Architecture for Target Detection

To evaluate the performance of different datasets, we are training two neural networks with the same architecture. The network parameters were tuned manually. The first network is exclusively trained and validated on synthetic data, while testing is conducted on real-world measurement data. The second network is trained and validated on a limited amount of measurement data, with testing performed on a separate set of measurement data. This setup allows us to assess the generalization capabilities and robustness of the models under varying noise and physical propagation conditions. This comparison helps assess the extent to which synthetic data can enhance model performance, particularly in scenarios with limited real-world data. The specific parameters for the CNN architectures are summarized in Table 9.

Table 9. CNN architecture and parameter configuration.

Parameter	CNN
Number of Convolutional Layers	2
Number of Pooling Layers	2
Kernel Size	(5×5)
Number of Filters	32/64
Activation Function	ReLU
Pooling Size	(2×2)
Pooling Type	Max Pooling
Dropout Rate	0.05
Batch Size	32
Learning Rate	0.001
Optimization Algorithm	Adam
Padding	Same

4. Results

The results are divided into two subchapters, Sections 4.1 and 4.2. Firstly, we evaluate our proposed workflow for generating synthetic data. We begin by capturing the fluctuation properties of the reflections in the measurements. In the second step, we present the results of our monostatic RCS simulation and compare the RCS variation with the fluctuation from the measurements. Subsequently, we investigate the impact of the target object's different

elevation and rotation angles on the strength and spatial distribution of the backscattered signals within the radar range map. This study highlights the sensitivity of measurements to minor angular variations. In the final subchapter, we compare the obtained range maps for RCS modeling and mesh modeling of the target with the measurement. The second chapter presents the results of detecting a dynamically moving target. The data composition and quality of the obtained synthetic data are primarily compared with the measured data. The prediction is first evaluated using a scatterplot of the ground truth and the prediction of the CNN to provide a qualitative overview of outliers. In the following chapter, a statistical evaluation is performed, and the probability of the prediction is evaluated based on the cumulative error distribution curve.

4.1. Evaluation of Synthetic Radar Data

4.1.1. Characterizing Radar Fluctuations Triggered by Small-Scale Human Movements

Due to the substantial heterogeneity of the RCS, minimal positional deviations, such as random body movements, can lead to deviations within the measured range profiles of a human [54]. This is why humans can be considered highly volatile targets in radar detection. The different range profiles during the measurement series are visualized in Figure 5, where the subject is positioned 2.0 m in front of the radar and stretches his hand toward the radar. The human can be seen in the measured range profile at a 2.0 m distance, and the hand is at a distance of approximately 1.5 m.

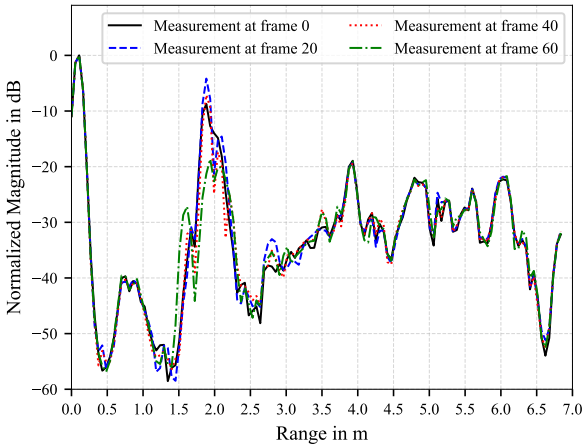
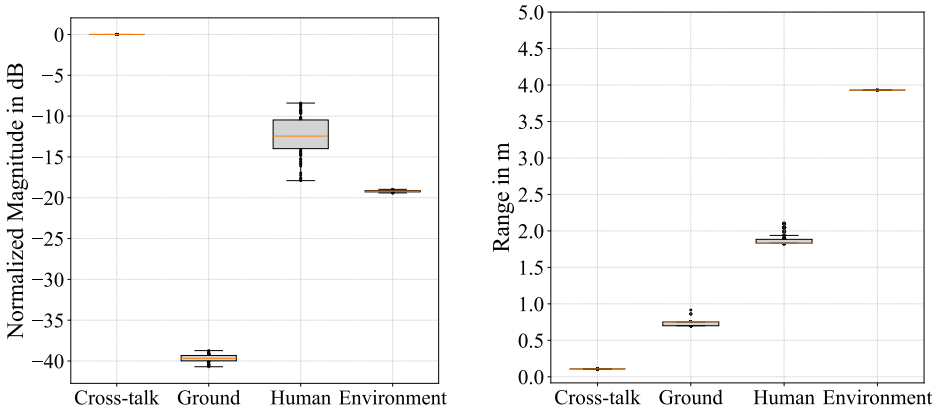


Figure 5. The 60 GHz radar range profile measured with a TI AWR6843 radar board showcasing the inherent noise and variability at millimeter-wave frequencies with a 3.99 GHz bandwidth (reprinted with permission from [12] 'IEEE 2024').

The measurement series was recorded with a frame rate of 5 Hz, where only four selected time steps are shown to visualize the dynamics of the radar channel. The range samples at 2 m reveal that reflections of the human fluctuate considerably. These results are consistent with the investigations from Abadpour in [16], where a static human showed an approximate variance of 5 dB, and while running, a variance of up to approximately 40 dB in measurements. The human target creates a prominent peak in the range profile, higher than static clutter. However, the magnitude of this peak fluctuates substantially from frame to frame, which can be attributed to the highly variable RCS of the human body. Furthermore, if two scatterers are close enough together, their responses are not resolved and instead blur into a single point, making it difficult to distinguish between them. On the other hand, environmental reflections are predominantly constant, with only minimal deviations across the measurements. The peak at approximately 0.75 m can be explained by a ground reflection. As shown in Figure 3, the antenna pattern of the patch antenna has a strong sidelobe that points toward the ground in an up-tilt radar configuration. This makes the radar very sensitive to ground reflections. Static reflection peaks can also be seen at

a distance from 3.0 m to 7.0 m. Where reflections caused by the surroundings are mainly constant, the high peak at approximately 0.1 m can be explained by constant cross-talk between the transmitting and receiving antennas [55,56].

To classify fluctuations over several measurement series, 85 frames were recorded, corresponding to an observation time of 17 s. The significant targets, i.e., cross-talk, ground, human, and environment, were statistically evaluated to describe the statistical behavior of strongly fluctuating targets over the entire measurement series. The normalized magnitude and the deviations in range directions are represented in Figure 6 by a boxplot, whereby each measurement point is also noted as a scatter plot, and the median is marked in orange. This type of evaluation allows statistical outliers to be better described and the simulation to be better matched with the measurement without coincidental matches between the simulation and measurement.



(**a**) Magnitude Variation Across Targets (**b**) Range Variation Across Targets

Figure 6. Comparison of variations in (**a**) magnitude and (**b**) range across different targets, demonstrating the significant fluctuations observed in both parameters during a static measurement.

4.1.2. Simulative Monostatic Radar Cross Section Analysis of Human Reflections

Substantial variations of the RCS can cause high dynamics in the range profile. This subchapter compares the dependencies between measurements and simulation results of the RCS in more detail.

Human reflections exhibit significant fluctuations due to their highly variable RCS. This results in a magnitude deviation of approximately 10 dB and a variation in range determination through peak detection of approximately 0.5 m. The substantial variation in the range profile can be explained primarily by different reflection angles between the human and the radar. These varying angles can redirect reflections from the torso to the head or other body parts, causing deviations of this magnitude. Figure 7 shows the calculated RCS deviations, with individual values presented rather than averaged. Figure 7 also shows that the RCS varies by approximately 20 dBm^2. The RCS later used for ray tracing was averaged again with a mean averaging filter of 2°.

4.1.3. Angular Dependence of Human Range Profiles

In addition to deviations caused by the RCS, different range profiles can also occur due to deviations in the up-tilt configuration of the radar board. The radar's up-tilt angle largely influences the proposed setup's signal-to-clutter ratio. To investigate the influence of the inclination angle of the board, three up-tilt angles, 17°, 20°, and 23°, are analyzed in Figure 8. At each angle, the human is turned in 4° steps starting from 0° to 12° around its z-axis to investigate deviations in the azimuth angle of the human. The simulation at this point is carried out using conventional ray tracing without considering RCS results.

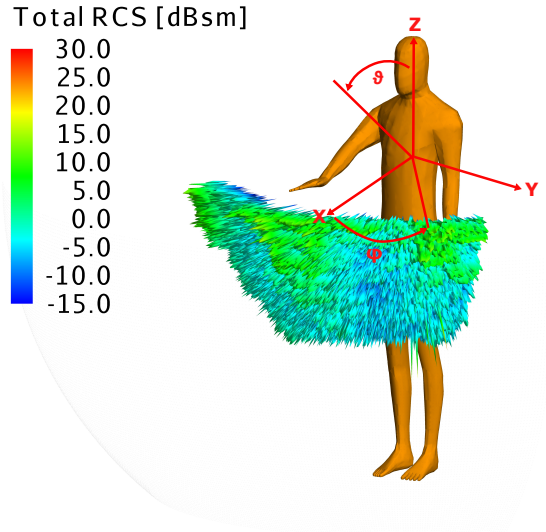


Figure 7. Analysis of the RCS variation of a human target at 60 GHz, considering the impact of orientation and body posture (reprinted with permission from [12] 'IEEE 2024').

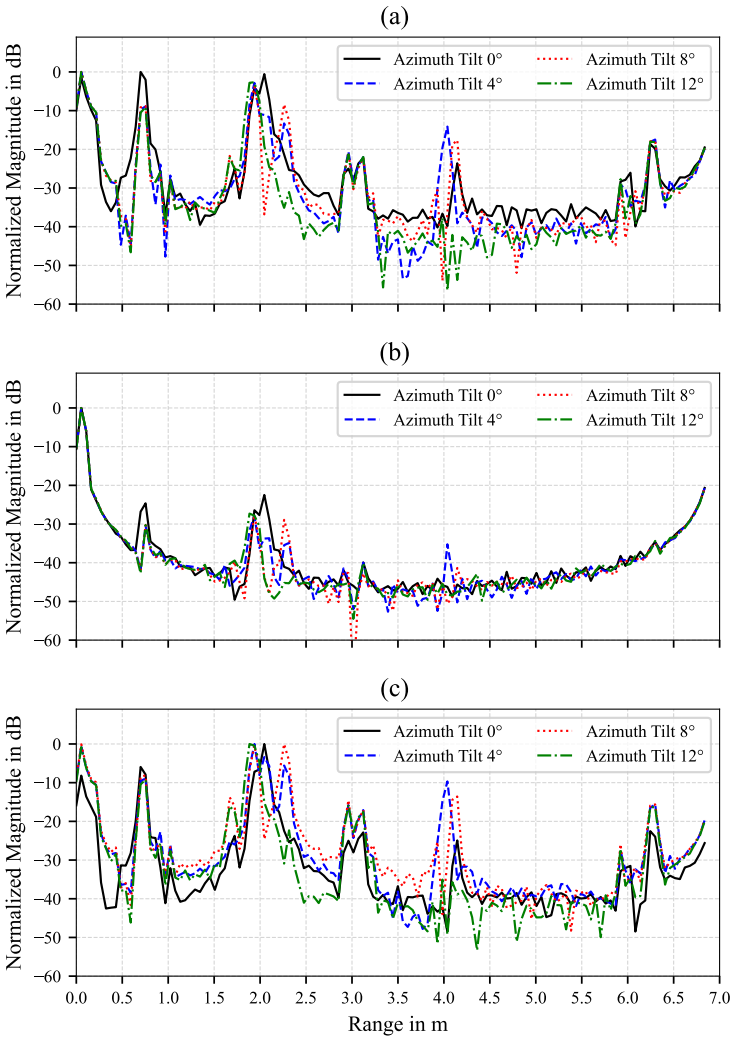


Figure 8. Simulation of different up-tilts angles with a rotation of the human target of (**a**) $\phi = 17°$, (**b**) $\phi = 20°$, (**c**) $\phi = 23°$ (reprinted with permission from [12] 'IEEE 2024').

The signal strength of the nearest reflection at approximately 0.2 m varies depending on the up-tilt configuration. This effect is caused by the strong sidelobe in the elevation direction. In addition, a pedestrian's rotation leads to significant differences in the peak's amplitude and range bin. The simulations show that slight differences in the orientation angle can cause variation in the human reflections in the measurement series. On the other hand, the up-tilt of the board primarily influences the ratio of the reflection strength between the human and the ground reflection. Depending on the human's rotation and tilt angle of the radar, the ratio of the human's reflection to the ground's reflection can vary by up to 10 dB. The simulations show that detection can vary greatly depending on the angle at which the radar board is mounted. The inclination angle should be adapted to the corresponding target height and distance for optimal detection. Furthermore, an optimized antenna pattern should be used to avoid sidelobes and prevent false detections.

4.1.4. Validating RCS and Mesh Target Modeling Through Measurements

After correlating the deviations in measurement results with the radar cross section and clarifying the impact of different inclination angles, the next stage involves comparing the measurements with simulations with the ray tracing and the RCS profile. Given that the inclination angle determined in the measurements may experience minor deviations, the simulation result of the ray tracing from Figure 9 was manually selected with the best possible match. The best match is achieved when the optimal signal-to-noise and clutter ratio between the human target's torso peak and the surrounding environment.

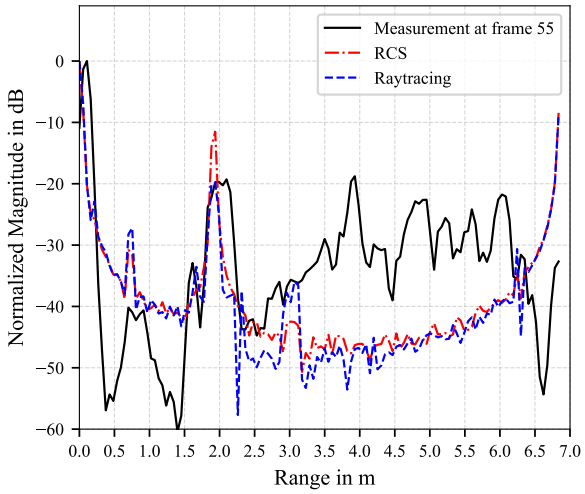


Figure 9. Comparison of simulation results with and without the use of RCS with the measured range profile (up-tilt radar: 23° and azimuth tilt of human: $\phi = 12°$) (reprinted with permission from [12] 'IEEE 2024').

Integration of the RCS profile results in an approximate increase in the signal-to-clutter ratio (SCR) by 8 dB, bringing it closer to the measured values. In addition, the human torso profile generally appears slightly more expansive in the RCS simulation due to increased mesh accuracy.

The calculation of the RCS is based on a monostatic approach, leading to the exclusion of multiple reflections. This aspect becomes particularly relevant in detecting humans, where multipath reflections are prominent, often resulting in a less distinct target peak. This effect is apparent in the simulations presented. While the simulation incorporating the RCS profile achieves a more accurate SCR ratio, aligning better with actual measurements, it fails to account for multipath phenomena. Overall, the signal strength of the human object in the RCS simulation is 10 dB higher than the measurement. However, it is difficult to precisely quantify the deviation in a single number, as shown in the previous chapters. The backscatter behavior fluctuates significantly between individual frames and depends on the

exact rotation angle. Since the reflection of human limbs is often dominated by multipath propagation at 60 GHz, the individual detection of a limb is limited. Discrepancies observed between the simulation and actual measurements, especially at greater distances, can be attributed to the finite number of rays computed in the simulation. As the distance from the radar increases, the energy density in the simulation decreases due to the spreading of rays. Consequently, any clutter effects that arise are only partially represented in the simulation, leading to these additional deviations.

4.2. Performance Evaluation of Synthetic Data in Convolutional Neural Networks

4.2.1. Dataset Composition and Structure

The quality and quantity of the dataset significantly impact the model performance. We partitioned our dataset into training, validation, and testing subsets. The training and validation sets are used to train the model, while the unseen test set is used for evaluation. We employed two primary approaches: (1) training (9000 samples) and validating on synthetic data (4500 samples) and testing on real-world measurement data (500 samples), and (2) splitting the measurement data into 70/30 training-validation split and a testing set (500 samples). The test set maintains a fixed size of measurement data, while the quantity of data in the training and validation sets varies. When generating the synthetic dataset, the target person moves into the farthest corners of the room and reduces the distance to the radar to just a few centimeters. The evaluation is presented as a box plot in Figure 10. The measurement datasets are mostly homogeneously shuffled. The mean of the datasets approximately matches that of the test dataset—however, a more significant deviation in the mean for the dataset with 100 measurements results from stochastic variation. The upper and lower deviations of the datasets match the test dataset. The range in which the labeled ground truth values are found slightly exceeds that of the test dataset. The average deviation is approximately 0.87 m below that of the test dataset. Overall, the synthetic dataset contains 13,500 samples. The box plot in Figure 10 illustrates the range distribution for datasets, showing the median values for each dataset: 100 samples (4.16 m), 200 samples (5.10 m), 300 samples (5.07 m), 400 samples (5.36 m), 500 samples (4.92 m), synthetic data with 13,500 samples (4.18 m), and test data with 500 samples (5.05 m).

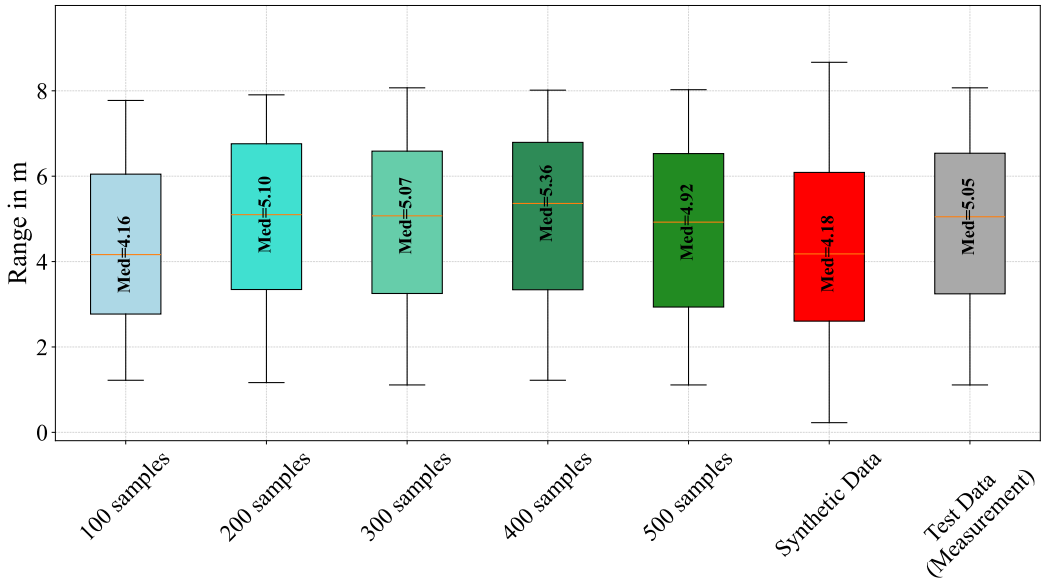
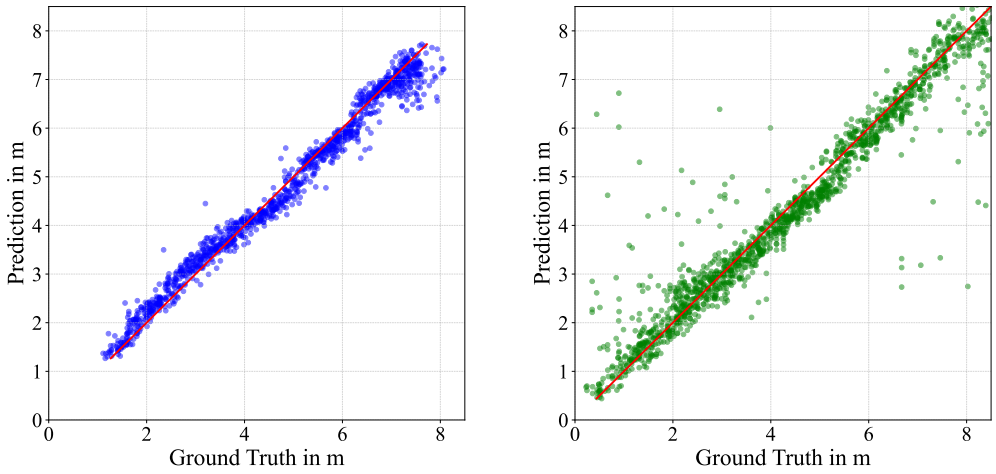


Figure 10. Box plot comparison of target range distribution to the radar across measurement, synthetic, and test datasets. The measurement datasets consist of 100 to 500 samples, split into training and validation sets with a 70/30 ratio, and were evaluated on the 500-sample test dataset.

4.2.2. Evaluation of Synthetic and Measurement Data Performance

To evaluate the CNN model and the dataset, we first analyze the ML model trained only on synthetic data. This model encountered no measurement data throughout the training and validation process. The synthetic data included higher noise variation than the measurement data to ensure robustness against changing noise conditions. The results of testing on unseen synthetic data are presented in Figure 11b. The agreement trend between the ground truth range values and the predicted range is visible. However, the model still exhibits several outliers with significant prediction deviations. The outliers can be attributed to the high noise floor and multipath configuration. In contrast, Figure 11a displays the CNN's range predictions trained purely on synthetic data and tested on labeled measurement data. It behaves significantly more robustly concerning outliers in the range detection, with a maximum deviation of approximately 1.0 m. Deviations of this magnitude occur in only 12 of the total 1214 samples. The outliers in the prediction of the simulated data are not due to CNN performance losses but rather to highly noisy signals. In some cases, the simulation data were deliberately subjected to harsh noise conditions to train the CNN as robustly as possible. The scatter plot demonstrates that the model trained on synthetic datasets performs reliably. When evaluated with measurement data, the model's prediction deviations were less frequent and more negligible, indicating a successful generalization from synthetic to real-world data. In summary, the CNN model trained on synthetic data demonstrates effective performance and robustness, mainly when applied to measurement data, underscoring the value of high-variation synthetic data in training robust machine learning models.



(**a**) Real environment (**b**) Simulation environment

Figure 11. Comparison of ground truth and CNN predictions validated on (**a**) real environment data and (**b**) synthetic data, indicating the model's performance in predicting target positions in real and simulated conditions with the regression line in red.

4.2.3. Cumulative Error Distribution

In addition to the qualitative evaluation of the results, Figure 12 presents the cumulative error deviation for different training datasets. In this study, we define the robustness of our ML model through the cumulative error deviation function, which represents the model's resilience to more significant outliers in range prediction. The evaluation is performed for measurement datasets containing 100 to 500 samples and the synthetic dataset. A cumulative error frequency plot against absolute error shows the CNN's performance across various datasets.

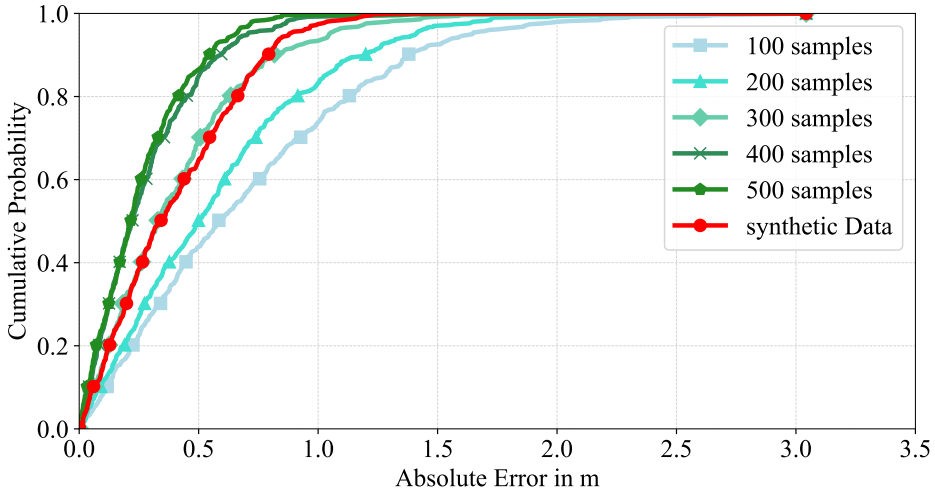


Figure 12. Absolute error distribution across datasets with varying sample sizes and full synthetic datasets.

Figure 12 demonstrates that the model's performance, measured by the frequency of significant error deviations, improves with more extensive data samples. In the training set with a sample size of 100, 25% of the predictions exhibit an absolute error deviation greater than 1 m. These deviations decrease significantly with sample sizes of 400 and 500, where such deviations become minimal. The synthetically generated dataset contains very few instances with an error deviation exceeding 1 m.

Table 10 provides quantitative results from Figure 12, showing the mean absolute error (MAE) and the root mean square error (RMSE) for CNN models trained on different datasets. The MAE decreases as the size of the dataset increases. Specifically, the synthetically generated dataset achieves an MAE of 0.397 m and an RMSE of 0.487 m, which are comparable to the values obtained with a dataset of 300 samples. This suggests that increasing the sample size enhances generalization and robustness. Furthermore, the results indicate that the model effectively transfers learning from purely synthetic datasets to measured datasets. Nonetheless, synthetic datasets may still have inherent quality limitations compared to datasets obtained directly from measurements.

Table 10. Performance metrics for standard ray tracing simulations across different datasets.

Dataset	MAE in m	RMSE in m
100 samples	0.698	0.875
200 samples	0.575	0.720
300 samples	0.407	0.527
400 samples	0.279	0.365
500 samples	0.257	0.331
Synthetic data	0.397	0.487

5. Discussion

This paper presents a data pipeline for simulating radar data based on a physical simulation of the electromagnetic propagation characteristics of 60 GHz millimeter waves. Sionna, Ansys, Remcom, or Winprop are tools for millimeter waves that offer ray tracing and are suitable for radar simulation. This WinProp-based approach successfully reproduces fundamental physical properties, such as multipath propagation via ground reflection, and even captures significant features like detecting body limbs. While a monostatic RCS simulation can achieve a significantly higher resolution by considering RF properties, it is only beneficial when multipath propagation from the main target plays a minor role. Incorporating bistatic RCS information would enable a more detailed consideration of

multipath propagation effects within the simulation framework. This extension could help overcome the limitations of complex reflection scenarios in indoor environments, as bistatic RCS allows for modeling signal paths that interact with multiple surfaces before returning to the receiver. This addition would lead to more precise modeling of the wave propagation effect, enhancing the accuracy of the object's reflection behavior and reducing simulation time. Bistatic RCS information has already been incorporated into ray tracing in [57,58]. Conversely, it leads to longer simulation times, as the calculations are significantly more complex than monostatic RCS. However, it is still being determined whether a higher level of information can be achieved compared to conventional mesh modeling since, in dynamic simulations, the RCS can fluctuate significantly, and the limitations are more related to the dynamic geometric dimensions. For machine learning, the geometric propagation of reflections is particularly important as it represents the features of objects. This can already be achieved through simple mesh modeling of the object. Mesh modeling of target objects provides a good balance, offering high resolution and sufficiently representative results for radar data generation. Integrating antenna patterns into ray tracing allows for accurate replication of the radar channel, including its sidelobe effects. Different tilt angles of the radar board and the object strongly influence the reflection behavior. The simulation accurately predicted the measurements for the static object. However, it did not fully capture the clutter level observed in the real-world data. While detecting moving objects is the primary goal, replicating the exact clutter value within range-Doppler maps is often unnecessary, as the focus lies on capturing the dynamic object behavior. Fluctuating noise values between measurements and strongly fluctuating reflection behavior make determining the exact noise floor difficult. Non-linear noise components can arise from hardware imperfections, such as non-linear distortion in amplifiers, mixer noise, ADC noise, or intermodulation products between several components [59–62]. To simplify the simulation and focus on extracting machine learning features relevant for moving object detection, non-linear noise components of the electronic radar components and the broadband propagation characteristics of the 60 GHz waves were not explicitly modeled.

The limitations of synthetic data in radar simulations arise from the simplifications in high-frequency simulations. While real-world wave propagation is continuous, simulations use ray tracing, which models discrete rays and cannot fully replicate the smooth behavior of electromagnetic waves. Natural environments with complex geometries and varying material properties are also challenging to simulate accurately. For example, natural materials exhibit changing electromagnetic properties depending on conditions like humidity and temperature, which are often simplified. The studies conducted by [63] revealed that the permittivity at 60 GHz can vary by up to 52% due to an air gap between the skin and the textile, making it extremely difficult to replicate in simulations. Interference and multipath interactions in dense environments also present challenges, as real-world scenarios involve intricate reflections and scattering that are hard to model precisely. Another limitation is replicating hardware components like filters, mixers, and amplifiers, which introduce noise and non-linearities in systems. In [64], the deterioration of signal quality due to non-linearities is investigated. These deviations are challenging to simulate fully. The systematic phase errors were studied in detail in [65] but are often assumed as additive white Gaussian noise as it is complex to reproduce the noise of the hardware in simulations exactly. The dynamic behavior of moving objects, such as slight deformations or variable radar cross-sections, is often inadequately modeled, especially for human targets. The investigations from Abadpour showed that the RCS at 77 GHz of the human torso can fluctuate by around 25 dB during movement and that of limbs by around 40 dB. Antenna design and radiation patterns can be accurately modeled, aiding optimization before real-world testing. The signal processing chain, including operations like FFT and Doppler analysis, is identical between synthetic and natural setups. Wave propagation is well simulated in plain environments with fewer objects, as ray tracing captures critical reflections and transmissions. Despite challenges in modeling complex environments and hardware, simulations remain valuable for design and testing, especially when real-world

measurements are difficult or costly. The proposed simulation framework represents key features like channel spread, noise floor, and signal strength, making simulations a reliable foundation for designing and developing algorithms for radar systems. The presented simulation framework can be extended to frequencies ranging from 300 MHz to 100 GHz. The ITU provides data on the electrical properties of materials, and the propagation model is applicable within this frequency range [48]. Various propagation simulations with this simulation framework at different frequencies have been investigated in [66].

In image processing with deep learning, it is common practice to synthesize large amounts of data to generate better generalizability. Researchers in [67–70] have already increased deep learning performance with synthetic data sets. The paper's results show that the model trained on synthetic datasets delivered particularly robust results in predicting range-Doppler maps despite the limited availability of real measurement data. The synthetic data demonstrated comparable performance to models trained on real data. Notably, with just 300 synthetic samples, a similar level of accuracy was achieved as with real measurement data, highlighting the effectiveness of the simulated datasets. When tested on real data, the CNN trained exclusively on synthetic data showed good generalization ability, with minimal deviations in range-Doppler profile predictions. In [71], the authors demonstrated that distributed radar measurements produce a heterogeneous dataset, affecting the learning process of deep learning algorithms. In particular, large and heterogeneous datasets have shown an enhanced ability to generalize. These findings align with existing literature. Dong and Liu have shown in [33] that ML models can be successfully trained on synthetic datasets through EM simulations for posture tracking. In [31], Sligar explored classifying various traffic participants using synthetic data. In our setup, the synthetic datasets exhibited higher variability, leading to more stable and robust predictions, especially in scenarios with multiple reflection paths and noise influences, which were simulated in the model. The cumulative error distribution indicated that the model trained with synthetic data had fewer larger errors, as the simulated scenarios covered a wide range of possible reflection and noise conditions. Overall, the use of synthetic datasets proved capable of enhancing the performance of ML models, particularly in terms of robustness to multiple reflections and noise, which are not only always captured in real measurement data. However, this work needed to include the transfer of results to real scenarios and model evaluation based on measurement data. Hybrid approaches combining synthetic and measurement data often present a promising strategy, as demonstrated in references [25,26]. However, these approaches are usually limited to selected scenarios and require a certain extent of measurement data. This research highlights the potential of synthetic data augmentation to enhance the performance of convolutional neural networks in radar-based applications. Similar to rendering techniques for image data augmentation, we demonstrate the effectiveness of simulating electromagnetic wave propagation to generate diverse training data for CNNs.

6. Conclusions

This paper investigates the potential of synthetic data to train robust CNN models. The simulation steps are illustrated, starting with the patch antenna simulation and proceeding through the physical propagation properties of millimeter waves to signal processing. Two distinct target modeling approaches are examined: monostatic RCS-based and mesh-based. Although monostatic RCS modeling provides more detail and incorporates interference characteristics of millimeter waves, indoor radar applications primarily rely on multipath propagation effects, which are not fully captured by monostatic RCS calculations using WinProp. Therefore, mesh-based modeling showed promising results as a more efficient approach for target representation in such scenarios. The results demonstrate that mesh-based modeling combined with ray tracing, considering the propagation effects of millimeter waves, produces range maps closely aligned with measured data. While the finite number of rays limits the environmental clutter representation, this constraint is generally acceptable, as object detection primarily focuses on key object features and not static

clutter representation. Measurements show that the reflection strength of human objects can fluctuate significantly, with variations of up to 10 dB observed in both measurements and simulations. This variability complicates direct comparisons between simulated and measured data. Accurate feature representation is crucial for machine learning applications, and significant reflections must be captured. Ray tracing provides a reliable method for reproducing human targets' most important reflection paths. The results show that ray tracing combined with mesh modeling can reproduce essential geometrical details of human poses. The static simulation results are extended to a dynamic scenario to evaluate the performance of the developed machine learning model on the range detection of a moving target. The generated dataset was compared with various measured datasets containing 100, 200, 300, 400, and 500 samples. The results demonstrate that machine learning performance depends on the dataset's variance and size. The synthetic dataset outperformed the measured dataset for sample sizes up to 300. Future work can focus on using the presented data pipeline for data augmentation in various radar applications. The pipeline offers significant advantages, especially for fast generation and large data labeling. In addition, its flexibility could support the development of robust models in different radar scenarios. Furthermore, how the generated data can be effectively used and integrated into different model architectures could be investigated.

Author Contributions: Conceptualization, P.R. and T.M.; methodology, P.R.; software, P.R. and T.M.; validation, P.R. and T.M.; formal analysis, P.R., J.B., and T.M.; investigation, P.R.; resources, P.R.; data creation, P.R.; writing—original draft preparation, P.R.; writing—review and editing, P.R., T.M., and J.B.; visualization, P.R. and T.M.; supervision, N.F. and M.L.; project administration, M.L. and N.F. All authors have read and agreed to the published version of the manuscript.

Funding: This work was supported by the Federal Ministry of Education and Research, Germany [Bundesministerium für Bildung und Forschung (BMBF)] as part of the project "6G-Access, Network of Networks, Automation & Simplification (6G-ANNA)" under Contract 16KISK084. The authors would like to acknowledge the use of OpenAI's ChatGPT to assist with grammar and language refinement in preparing this manuscript.

Data Availability Statement: The data presented in this study are available on request from the corresponding author, the data are not publicly available due to privacy.

Conflicts of Interest: The authors declare no conflicts of interest.

References

1. Wang, P. Research on Comparison of LiDAR and Camera in Autonomous Driving. *J. Phys. Conf. Ser.* **2021**, *2093*, 012032. [CrossRef]
2. Mielle, M.; Magnusson, M.; Lilienthal, A.J. A comparative analysis of radar and lidar sensing for localization and mapping. In Proceedings of the 2019 European Conference on Mobile Robots (ECMR), Prague, Czech Republic, 4–6 September 2019; pp. 1–6. [CrossRef]
3. Bilik, I. Comparative Analysis of Radar and Lidar Technologies for Automotive Applications. *IEEE Intell. Transp. Syst. Mag.* **2023**, *15*, 244–269. [CrossRef]
4. Hoffmann, M.; Kunzmann, G.; Dudda, T.; Irmer, R.; Jukan, A.; Macher, G.; Ahmad, A.; Beenen, F.R.; Bröring, A.; Fellhauer, F.; et al. A Secure and Resilient 6G Architecture Vision of the German Flagship Project 6G-ANNA. *IEEE Access* **2023**, *11*, 102643–102660. [CrossRef]
5. Albuquerque, D.; Cruz, B.; Gouveia, C.; Coelho, V.; Pinho, P.; Matos, J.; Oliveira, A.; Carvalho, N. Indoor Near-Field Impact in the RADAR Signals for 6G Mobile Networks Integration. In Proceedings of the 2022 13th International Symposium on Communication Systems, Networks and Digital Signal Processing (CSNDSP), Porto, Portugal, 20–22 July 2022; pp. 310–313. [CrossRef]
6. Yang, Y.; Wang, Y.; Zheng, B.; Yi, X.; Che, W.; Xue, Q. Challenges of Joint Radar-Communication Front-End for 6G Applications. In Proceedings of the 2021 IEEE International Workshop on Electromagnetics: Applications and Student Innovation Competition (iWEM), Guangzhou, China, 28–30 November 2021; Volume 1, pp. 1–3. [CrossRef]
7. Zhang, A.; Nowruzi, F.E.; Laganiere, R. RADDet: Range-Azimuth-Doppler based Radar Object Detection for Dynamic Road Users. In Proceedings of the 2021 18th Conference on Robots and Vision (CRV), Burnaby, BC, Canada, 26–28 May 2021; pp. 95–102. [CrossRef]
8. Srivastav, A.; Mandal, S. Radars for Autonomous Driving: A Review of Deep Learning Methods and Challenges. *IEEE Access* **2023**, *11*, 97147–97168. [CrossRef]

9. Neekzad, B.; Sayrafian-Pour, K.; Perez, J.; Baras, J.S. Comparison of Ray Tracing Simulations and Millimeter Wave Channel Sounding Measurements. In Proceedings of the 2007 IEEE 18th International Symposium on Personal, Indoor and Mobile Radio Communications, Athens, Greece, 3–7 September 2007; pp. 1–5. [CrossRef]
10. Placidi, S.; Vetere, A.; Pino, E.; Meta, A. Advanced SAR simulator for ATR and AI database generation. In Proceedings of the 2021 7th Asia-Pacific Conference on Synthetic Aperture Radar (APSAR), Bali, Indonesia, 1–3 November 2021; pp. 1–6. [CrossRef]
11. Nguyen Ngoc, T.M.; Linh, M.; Dinh Uyen, N.; Van Su, T. A 3D model to characterize EM far-field scattering and its applications in SAR data synthesis. In Proceedings of the 2015 International Conference on Advanced Technologies for Communications (ATC), Ho Chi Minh City, Vietnam, 14–16 October 2015; pp. 633–636. [CrossRef]
12. Reitz, P.; Maiwald, T.; Franchi, N.; Weigel, R.; Lübke, M. Evaluating Synthetic Data Potential for 60 GHz FMCW Radar Simulations with Measurements. In Proceedings of the 2024 International Radar Symposium (IRS), Wroclaw, Poland, 2–4 July 2024; pp. 129–134.
13. Schöffmann, C.; Ubezio, B.; Böhm, C.; Mühlbacher-Karrer, S.; Zangl, H. Virtual Radar: Real-Time Millimeter-Wave Radar Sensor Simulation for Perception-Driven Robotics. *IEEE Robot. Autom. Lett.* **2021**, *6*, 4704–4711. [CrossRef]
14. Stetco, C.; Ubezio, B.; Mühlbacher-Karrer, S.; Zangl, H. Radar Sensors in Collaborative Robotics: Fast Simulation and Experimental Validation. In Proceedings of the 2020 IEEE International Conference on Robotics and Automation (ICRA), Paris, France, 31 May–31 August 2020; pp. 10452–10458. [CrossRef]
15. Schouten, G.; Jansen, W.; Steckel, J. Simulation of Pulse-Echo Radar for Vehicle Control and SLAM. *Sensors* **2021**, *21*, 523. [CrossRef]
16. Abadpour, S. Modeling Backscattering Behavior of Vulnerable Road Users Based on High-Resolution Radar Measurements. Ph.D. Thesis, KIT Scientific Publishing, Karlsruhe, Germany, 2023. [CrossRef]
17. Belgiovane, D.; Chen, C.C.; Chen, M.; Chien, S.Y.P.; Sherony, R. 77 GHz radar scattering properties of pedestrians. In Proceedings of the 2014 IEEE Radar Conference, Cincinnati, OH, USA, 19–23 May 2014; pp. 0735–0738. [CrossRef]
18. Hügler, P.; Geiger, M.; Waldschmidt, C. RCS measurements of a human hand for radar-based gesture recognition at E-band. In Proceedings of the 2016 German Microwave Conference (GeMiC), Bochum, Germany, 14–16 March 2016; pp. 259–262. [CrossRef]
19. Abadpour, S.; Marahrens, S.; Pauli, M.; Siska, J.; Pohl, N.; Zwick, T. Backscattering Behavior of Vulnerable Road Users Based on High-Resolution RCS Measurements. *IEEE Trans. Microw. Theory Tech.* **2022**, *70*, 1582–1593. [CrossRef]
20. Decker, J.; Saad, K.; Rey, D.; Canta, S.M.; Kipp, R.A. Physics-Based, Real-Time MIMO Radar Simulation for Autonomous Driving. In *Proceedings of the Automatisiertes Fahren 2021*; Bertram, T., Ed.; Springer Nature: Wiesbaden, Germany, 2021; pp. 83–93.
21. Schoeder, P.; Janoudi, V.; Meinecke, B.; Werbunat, D.; Waldschmidt, C. Flexible Direction-of-Arrival Simulation for Automotive Radar Target Simulators. *IEEE J. Microwaves* **2021**, *1*, 930–940. [CrossRef]
22. Yuan, S.; Fioranelli, F.; Yarovoy, A.G. Vehicular-Motion-Based DOA Estimation With a Limited Amount of Snapshots for Automotive MIMO Radar. *IEEE Trans. Aerosp. Electron. Syst.* **2023**, *59*, 7611–7625. [CrossRef]
23. Chipengo, U.; Krenz, P.; Carpenter, S. From Antenna Design to High Fidelity, Full Physics Automotive Radar Sensor Corner Case Simulation. *Model. Simul. Eng.* **2018**, *2018*, 4239725. [CrossRef]
24. Diewald, A. High-Precision Automotive Radar Target Simulation. Ph.D. Thesis, Institut für Hochfrequenztechnik und Elektronik (IHE), Karlsruhe, Germany, 2023. [CrossRef]
25. Kern, N.; Schoeder, P.; Waldschmidt, C. Virtually Augmented Radar Measurements with Hardware Radar Target Simulators for Machine Learning Applications. *IEEE Sens. Lett.* **2024**, *8*, 3500504. [CrossRef]
26. Moilanen, I.; Lintonen, T.; Kiviranta, M.; Sangi, P.; Pyhtilä, J.; Pirinen, P.; Juntti, M. Ray Tracing Assisted Radar Detection in 6G. In Proceedings of the 2023 IEEE 98th Vehicular Technology Conference (VTC2023-Fall), Hong Kong, China, 10–13 October 2023; pp. 1–6. [CrossRef]
27. Schuessler, C.; Zhang, W.; Bräunig, J.; Hoffmann, M.; Stelzig, M.; Vossiek, M. Radar-Based Recognition of Static Hand Gestures in American Sign Language. In Proceedings of the 2024 IEEE Radar Conference (RadarConf24), Denver, CO, USA, 6–10 May 2024; pp. 1–6. [CrossRef]
28. Sengupta, A.; Jin, F.; Zhang, R.; Cao, S. mm-Pose: Real-Time Human Skeletal Posture Estimation Using mmWave Radars and CNNs. *IEEE Sens. J.* **2020**, *20*, 10032–10044. [CrossRef]
29. Cai, X.; Giallorenzo, M.; Sarabandi, K. Machine Learning-Based Target Classification for MMW Radar in Autonomous Driving. *IEEE Trans. Intell. Veh.* **2021**, *6*, 678–689. [CrossRef]
30. Orduyilmaz, A.; Yar, E.; Kocamis, M.B.; Serin, M.; Efe, M. Machine learning-based radar waveform classification for cognitive EW. *Signal Image Video Process.* **2021**, *15*, 1653–1662. [CrossRef]
31. Sligar, A.P. Machine Learning-Based Radar Perception for Autonomous Vehicles Using Full Physics Simulation. *IEEE Access* **2020**, *8*, 51470–51476. [CrossRef]
32. Waqar, S.; Muaaz, M.; Sigg, S.; Pätzold, M. A Paradigm Shift From an Experimental-Based to a Simulation-Based Framework Using Motion-Capture Driven MIMO Radar Data Synthesis. *IEEE Sens. J.* **2024**, *24*, 16614–16628. [CrossRef]
33. Dong, G.; Liu, H. A New Image Simulation Technique for Deep-Learning-Based Radar Target Recognition. *IEEE Trans. Instrum. Meas.* **2023**, *72*, 2512610. [CrossRef]
34. Schnattinger, G.; Baur, C.; Huber, B. Generating and Using Synthetic Data for Machine Learning in Personnel Security Screening Scenarios. In Proceedings of the 2023 20th European Radar Conference (EuRAD), Berlin, Germany, 20–22 September 2023; pp. 139–142. [CrossRef]

35. Zong, M.; Zhu, Z.; Wang, H. A Simulation Method for Millimeter-Wave Radar Sensing in Traffic Intersection Based on Bidirectional Analytical Ray-Tracing Algorithm. *IEEE Sensors J.* **2023**, *23*, 14276–14284. [CrossRef]
36. Zhou, Y.; Liu, L.; Zhao, H.; López-Benítez, M.; Yu, L.; Yue, Y. Towards Deep Radar Perception for Autonomous Driving: Datasets, Methods, and Challenges. *Sensors* **2022**, *22*, 4208. [CrossRef]
37. Zhou, Y. GitHub—ZHOUYI1023/Awesome-Radar-Perception: A Curated List of Radar Datasets, Detection, Tracking and Fusion, 2024. Available online: https://github.com/ZHOUYI1023/awesome-radar-perception (accessed on 23 October 2024).
38. Herda, D.L.; Suryana, J.; Izzuddin, A. Radar Cross Section of F35: Simulation and Measurement. In Proceedings of the 2020 6th International Conference on Wireless and Telematics (ICWT), Yogyakarta, Indonesia, 3–4 September 2020; pp. 1–6. [CrossRef]
39. PREDICS. Radar Cross Section (RCS) Simulation Validations via Benchmark Objects. 2024. White Paper. Available online: https://predicsrcs.com/themes/base/assets/image/predics/whitePapers/PREDICS_WP1_RCS%20OF%20BENCHMARK%20OBJECTS.pdf (accessed on 23 October 2024).
40. Corbel, C.; Bourlier, C.; Pinel, N.; Chauveau, J. Rough Surface RCS Measurements and Simulations Using the Physical Optics Approximation. *IEEE Trans. Antennas Propag.* **2013**, *61*, 5155–5165. [CrossRef]
41. Potgieter, M.; Odendaal, J.W.; Blaauw, C.; Joubert, J. Bistatic RCS Measurements of Large Targets in a Compact Range. *IEEE Trans. Antennas Propag.* **2019**, *67*, 2847–2852. [CrossRef]
42. Pienaar, M.; Odendaal, J.W.; Joubert, J.; Pienaar, C.; Smit, J.C. Bistatic RCS measurements in a compact range. In Proceedings of the 2017 International Conference on Electromagnetics in Advanced Applications (ICEAA), Verona, Italy, 11–15 September 2017; pp. 1199–1202. [CrossRef]
43. Lübke, M.; Fuchs, J.; Dubey, A.; Hamoud, H.; Dressler, F.; Weigel, R.; Lurz, F. Validation and Analysis of the Propagation Channel at 60 GHz for Vehicular Communication. In Proceedings of the 2021 IEEE 94th Vehicular Technology Conference (VTC2021-Fall), Norman, OK, USA, 27–30 September 2021; pp. 1–7. [CrossRef]
44. Altair. User Guide Objects. 2024. Available online: https://help.altair.com/feko/pdf/Altair_Feko_User_Guide.pdf (accessed on 23 October 2024).
45. Chen, M.; Chen, C.C. RCS Patterns of Pedestrians at 76–77 GHz. *IEEE Antennas Propag. Mag.* **2014**, *56*, 252–263. [CrossRef]
46. Yamada, N.; Tanaka, Y.; Nishikawa, K. Radar cross section for pedestrian in 76GHz band. In Proceedings of the 2005 European Microwave Conference, Paris, France, 4–6 October 2005; Volume 2, pp. 4–1018. [CrossRef]
47. Marchetti, E.; Du, R.; Willetts, B.; Norouzian, F.; Hoare, E.; Tran, T.; Clarke, N.; Cherniakov, M.; Gashinova, M. Radar cross-section of pedestrians in the low-THz band. *IET Radar Sonar Navig.* **2018**, *12*, 1104–1113. [CrossRef]
48. International Telecommunication Union. *Effects of Building Materials and Structures on Radiowave Propagation Above About 100 MHz*; Technical Report P.2040-2, ITU-R; International Telecommunication Union: Geneva, Switzerland, 2021.
49. Dielectric Properties of Body Tissues. Home Page. Available online: http://niremf.ifac.cnr.it/tissprop/#refs (accessed on 23 October 2024).
50. Alekseev, S.; Radzievsky, A.; Logani, M.; Ziskin, M. Millimeter wave dosimetry of human skin. *Bioelectromagnetics* **2008**, *29*, 65–70. [CrossRef] [PubMed]
51. Dham, V. *Programming Chirp Parameters in TI Radar Devices*; Application Report; Texas Instruments: Dallas, TX, USA, 2020.
52. Carlson, A.B.; Crilly, P.B. *Communication Systems*; McGraw-Hill Higher Education: New York, NY, USA, 2010.
53. Richards, M.A. *Fundamentals of Radar Signal Processing*, 3rd ed.; McGraw-Hill Education: New York, NY, USA, 2022; p. 701.
54. Yang, Z.K.; Shi, H.; Zhao, S.; Huang, X.D. Vital Sign Detection During Large-Scale and Fast Body Movements Based on an Adaptive Noise Cancellation Algorithm Using a Single Doppler Radar Sensor. *Sensors* **2020**, *20*, 4183. [CrossRef]
55. Lei, P.; Yu, Q.; Wang, J. Polynomial Fitting Based Crosstalk Suppression in the Monostatic FMCW Radar. In Proceedings of the 2019 IEEE 4th International Conference on Signal and Image Processing (ICSIP), Wuxi, China, 19–21 July 2019; pp. 284–288. [CrossRef]
56. Sacco, G.; Piuzzi, E.; Pittella, E.; Pisa, S. An FMCW Radar for Localization and Vital Signs Measurement for Different Chest Orientations. *Sensors* **2020**, *20*, 3489. [CrossRef]
57. Ebrahimizadeh, J.; Madannejad, A.; Cai, X.; Vinogradov, E.; Vandenbosch, G.A.E. RCS-Based 3-D Millimeter-Wave Channel Modeling Using Quasi-Deterministic Ray Tracing. *IEEE Trans. Antennas Propag.* **2024**, *72*, 3596–3606. [CrossRef]
58. Deep, Y.; Held, P.; Ram, S.S.; Steinhauser, D.; Gupta, A.; Gruson, F.; Koch, A.; Roy, A. Radar Cross-Sections of Pedestrians at Automotive Radar Frequencies Using Ray Tracing and Point Scatterer Modelling. *IET Radar Sonar Navig.* **2020**, *14*, 833–844. [CrossRef]
59. Dudek, M.; Nasr, I.; Kissinger, D.; Weigel, R.; Fischer, G. The impact of phase noise parameters on target signal detection in FMCW-radar system simulations for automotive applications. In Proceedings of the Proceedings of 2011 IEEE CIE International Conference on Radar, Chengdu, China, 24–27 October 2011; Volume 1, pp. 494–497. [CrossRef]
60. Lin, Y.S.; Lee, C.Y.; Chen, C.C. A 9.99 mW low-noise amplifier for 60 GHz WPAN system and 77 GHz automobile radar system in 90 nm CMOS. In Proceedings of the 2015 IEEE Radio and Wireless Symposium (RWS), San Diego, CA, USA, 25–28 January 2015; pp. 65–67. [CrossRef]
61. Baktir, C.; Sobaci, E.; Dönmez, A. A guide to reduce the phase noise effect in FMCW Radars. In Proceedings of the 2012 IEEE Radar Conference, Atlanta, GA, USA, 7–11 May 2012; pp. 0236–0239. [CrossRef]

62. Rengifo, S.C.; Chicco, F.; Le Roux, E.; Enz, C. Modulation Scheme Impact on Phase Noise in FMCW Radar for Short-Range Applications. In Proceedings of the 2021 IEEE International Symposium on Circuits and Systems (ISCAS), Daegu, Korea, 22–28 May 2021; pp. 1–4. [CrossRef]
63. Sacco, G.; Pisa, S.; Zhadobov, M. Impact of Textile on Electromagnetic Power and Heating in Near-Surface Tissues at 26 GHz and 60 GHz. *IEEE J. Electromagn. Microwaves Med. Biol.* **2021**, *5*, 262–268. [CrossRef]
64. Zheng, R.; Wang, C.; He, X.; Li, X. A Correction Method for the Nonlinearity of FMCW Radar Sensors Based on Multisynchrosqueezing Transform. *IEEE Sens. J.* **2023**, *23*, 609–619. [CrossRef]
65. Tschapek, P.; Körner, G.; Carlowitz, C.; Vossiek, M. Detailed Analysis and Modeling of Phase Noise and Systematic Phase Distortions in FMCW Radar Systems. *IEEE J. Microwaves* **2022**, *2*, 648–659. [CrossRef]
66. Reitz, P.; Künzle, C.; Franchi, N.; Lübke, M. Evaluation of the Interference Performance of FMCW Radar Sensors in Dense Indoor Environments. *IEEE Access* **2024**, *12*, 46834–46850. [CrossRef]
67. Mill, L.; Wolff, D.; Gerrits, N.; Philipp, P.; Kling, L.; Vollnhals, F.; Ignatenko, A.; Jaremenko, C.; Huang, Y.; Castro, O.D.; et al. Synthetic Image Rendering Solves Annotation Problem in Deep Learning Nanoparticle Segmentation. *Small Methods* **2021**, *5*, 2100223. [CrossRef] [PubMed]
68. Proença, P.F.; Gao, Y. Deep Learning for Spacecraft Pose Estimation from Photorealistic Rendering. In Proceedings of the 2020 IEEE International Conference on Robotics and Automation (ICRA), Paris, France, 31 May–31 August 2020; pp. 6007–6013. [CrossRef]
69. Man, K.; Chahl, J. A Review of Synthetic Image Data and Its Use in Computer Vision. *J. Imaging* **2022**, *8*, 310. [CrossRef]
70. Paulin, G.; Ivasic-Kos, M. Review and analysis of synthetic dataset generation methods and techniques for application in computer vision. *Artif. Intell. Rev.* **2023**, *56*, 9221–9265. [CrossRef]
71. Seo, J.; Yunji, Y.; Hong, Y.g.; Park, J. Transfer learning-based radar imaging with deep convolutional neural networks for distributed frequency modulated continuous waveform multiple-input multiple-output radars. *IET Radar Sonar Navig.* **2021**, *15*, 1209–1220. [CrossRef]

Disclaimer/Publisher's Note: The statements, opinions and data contained in all publications are solely those of the individual author(s) and contributor(s) and not of MDPI and/or the editor(s). MDPI and/or the editor(s) disclaim responsibility for any injury to people or property resulting from any ideas, methods, instructions or products referred to in the content.